Article

Exploring causes of distinct regional and subseasonal Indian summer monsoon precipitation responses to CO₂ removal

Check for updates

Seungmok Paik [1], Daehyun Kim [2,3] ✉, Soon-Il An [1,4,5] ✉, Hyoeun Oh[6,7], Jongsoo Shin[8],
Bidyut Bikash Goswami[9], Seung-Ki Min [5,10] & Sanjit Kumar Mondal[1]

This study investigates the response of Indian summer monsoon (ISM) precipitation to CO₂ removal, with a specific focus on regional and subseasonal variations. Following CO₂ removal, monsoon circulation weakens throughout the summer owing to the reduced large-scale meridional temperature gradient around India. Weakened monsoon circulation decreases the local-scale thermodynamic stability within India, following monsoon-onset periods. While the frequency of synoptic-scale ISM low-pressure systems (LPSs) decreases overall, the lower thermodynamic stability causes the LPSs to form and resultantly shift west and south from their typical paths, last longer and move more quickly zonally during August and September. Changes in these rain-producing processes induce distinct regional (Western Ghats, south-central-east India, and Tamil Nadu) and subseasonal precipitation responses. Also, extreme precipitation exhibits similar patterns, but is more strongly affected by changes in LPS. Our results suggest that reliable future projections of regional hydroclimate change require a more accurate understanding of multi-scale precipitation processes.

Global warming induced by anthropogenic greenhouse gases has accelerated and is projected to persist throughout the 21st century, contingent on the continuation of greenhouse gas emissions[1]. Changes in precipitation induced by global warming are among the most significant impacts of climate change, with both mean and extreme precipitation being expected to increase[2]. Significant increases in mean and extreme precipitation have already been observed during the historical period, which have been attributed to anthropogenic radiative forcing[3–5]. These observed trends are projected to persist throughout the 21st century under various greenhouse gas emission scenarios[6,7], which would likely lead to an increase in the intensity and frequency of hydroclimatic disasters, such as flooding.

Given the ongoing high levels of global greenhouse gas emissions[8], there has been growing interest in the concept of carbon dioxide (CO₂) removal (CDR) as a means of achieving the global warming mitigation targets established by the Paris Agreement in 2015[9]. With CDR being discussed as a possible global warming mitigation strategy, a wide range of questions regarding its consequences have been raised and addressed within the climate research community. In particular, studies have focused on

whether and to what extent, the climate system exhibits hysteresis in response to changes in radiative forcing associated with greenhouse gas concentrations (e.g., Kim et al.[10]). The emergence of hysteresis has been suggested in large-scale and low-frequency atmospheric and oceanic conditions/variabilities such as the Atlantic Meridional Overturning Circulation (AMOC), inter-tropical convergence zone, El Niño-Southern Oscillation (ENSO), Southern Ocean, and Hadley cell[11–18].

Beyond the hysteresis in large-scale phenomena, studies have also explored how global-to-regional precipitation varies with CDR. A slow recovery of global mean precipitation has been reported in response to CDR, which is primarily attributed to the accumulation of heat in the ocean[19]. Nearly symmetric and asymmetric precipitation changes have been found across global land and oceans, respectively, when comparing the CO₂ ramp-up and ramp-down periods[20]. Furthermore, the occurrence of regional mean and extreme precipitation hysteresis have been reported[10,21].

In the context of monsoons, a negative overshoot (i.e., the reduction surpasses its initial level) in Indian and North African summer monsoon precipitation following CDR has been reported[22], which was primarily

[1]Irreversible Climate Change Research Center, Yonsei University, Seoul, South Korea. [2]School of Earth and Environmental Sciences, Seoul National University, Seoul, South Korea. [3]Department of Atmospheric Sciences, University of Washington, Seattle, WA, USA. [4]Department of Atmospheric Sciences, Yonsei University, Seoul, South Korea. [5]Division of Environmental Science and Engineering, Pohang University of Science and Technology, Pohang, South Korea. [6]Center for Climate Physics, Institute for Basic Science, Busan, South Korea. [7]Pusan National University, Busan, South Korea. [8]Woods Hole Oceanographic Institution, Woods Hole, MA, USA. [9]Institute of Science and Technology Austria, Klosterneuburg, Austria. [10]Institute for Convergence Research and Education in Advanced Technology, Yonsei University, Incheon, South Korea. ✉e-mail: daehyun@snu.ac.kr; sian@yonsei.ac.kr

1

attributed to southward shifts of the inter-tropical convergence zone due to hysteresis in the AMOC and Southern Ocean[14]. In contrast, the amount of annual maximum daily precipitation, a commonly used representative index of extreme precipitation intensity, was found to exhibit no hysteresis when comparing the CO_2 ramp-up and ramp-down periods[22]. Other studies have recently reported a significant reduction in Indian summer monsoon (ISM) precipitation and delayed onset of the ISM with CDR[23,24], based on multiple climate model simulations from the Carbon Dioxide Removal Model Intercomparison Project (CDRMIP)[25]. In addition, hysteresis in summer monsoon precipitation and the frequency of extreme rainfall events have been suggested across East Asia[15,26], attributed to the emergence of El Niño-like warm conditions in the tropical Pacific with CDR. Furthermore, hysteresis in the global-to-regional monsoon area has been reported, along with associated features, which have been attributed to hysteresis in large-scale atmospheric and oceanic environmental conditions[27].

Among the global monsoon regions, India is particularly important for understanding hydroclimatic changes following CDR. It exerts a critical influence on a wide range of socioeconomic impacts, including agriculture and water resources, affecting more than one-sixth of the world's population under conditions of weak climate resilience. Previous studies on ISM precipitation within the context of CDR have commonly reported rapid recovery accompanied by a declining tendency and negative overshoot[22,23,27], inducing a delayed onset of the ISM during the CO_2 ramp-down period[24]. However, these analyses have limitations in providing projections at detailed spatial and temporal scales. While primarily focusing on the entirety of India with seasonal mean changes, they overlooked regional and subseasonal variations. Extending the exploration beyond region-wide and seasonal mean changes is essential, as a more comprehensive analysis of regional and subseasonal responses and associated monsoon features can provide valuable insights with significant implications for various socioeconomic systems across India, such as agriculture. Moreover, while the importance of ISM low-pressure systems (LPSs) in the hydroclimate across India has been well documented[28–30], their changes during the historical period and future projections are still under debate[31–38], and their changes under CDR have not been investigated.

To address these gaps in knowledge, our study assesses the responses of ISM precipitation to CDR, taking into account its spatial distribution and characteristics over a range of timescales from subseasonal to sub-daily. We utilized the Community Earth System Model version 1.2.2 (CESM1)[39] and conducted idealized CO_2 pathway simulations, encompassing atmospheric CO_2 concentration ramp-up, ramp-down and restoration (Methods). CESM1 realistically captures the observed overall subseasonal ISM characteristics (Supplementary Fig. 1). Our study diverges significantly from previous studies as we explore the role of synoptic-scale weather systems – ISM LPSs. This unique approach aims to provide an in-depth understanding of the spatially and temporally detailed hysteretic responses in ISM precipitation.

Results

ISM precipitation responses to CDR

Figure 1a presents the timeseries of atmospheric CO_2 concentration, annual-mean surface air temperature for the global, Northern Hemisphere (NH), and Southern Hemisphere (SH) averages, and ISM precipitation (averages from June to October) in the CESM1 simulations. The global mean temperature shows a slight delay but exhibits an overall linear response to CO_2 forcings, increasing during the CO_2 ramp-up period and decreasing under CO_2 ramp-down with a delay. This delayed recovery of the global mean temperature is due to slower cooling in the SH than in the NH. In contrast, the ISM precipitation displays robust hysteretic behavior, characterized by a negative overshoot during the CO_2 ramp-down period. We identify specific 50-year periods that demonstrate maximal precipitation hysteresis during the CO_2 ramp-down period (years 2231–2280), along with corresponding CO_2 ramp-up periods that present the same global warming levels (2035–2084), denoted by shading in Fig. 1a. The differences between these periods (2231–2280 subtracted from 2035–2084) will be

denoted as RD-RU henceforth. This approach has the advantage of investigating the climate differences between the CO_2 ramp-up and ramp-down periods under the same thermal conditions on Earth. This is suitable for understanding the impacts of CDR that are not caused by the difference in the global mean surface temperature.

Figure 1b illustrates the spatial pattern of ISM precipitation and the 850 hPa horizontal wind, averages from June to October in the RD-RU. Pronounced decreases in precipitation and weakening of ISM circulation (climatology is presented in Supplementary Fig. 1) are shown over India, which is consistent with previous studies[22,23,27]. However, it should be noted that precipitation responses are not spatially homogeneous across India, exhibiting the strongest decreases within the Western Ghats (left box) and south-central-east India (right upper box), while changes are insignificant in Tamil Nadu (the southernmost state of India; right lower box). We define the left box in Fig. 1b as 'Western Ghats' since precipitation in that area is concentrated along the Western Ghats. The right box in Fig. 1b is labeled 'south-central-east India' as it includes the northeastern part of south India, central and east India. The corresponding results during individual months (Fig. 1c–g) show interesting subseasonal variability, with more pronounced ISM precipitation reduction and easterly wind anomalies (i.e., weakening of monsoon westerlies) in June and July compared to those in later months. The spatial heterogeneity of precipitation responses is more pronounced in individual monthly responses, despite the general weakening of the ISM circulation across all months. Notably, in August, the Western Ghats show insignificant precipitation responses, while significant increases appear in its southern areas (Fig. 1e). Tamil Nadu exhibits increases or insignificant responses in precipitation from July to October (Fig. 1d–g). The spatio-temporal heterogeneity of the ISM precipitation responses in RD-RU suggests that the precipitation change may not simply be explained by the weakening of monsoon circulation. Rather, it is likely that precipitation in individual regions is influenced by diverse physical mechanisms, such as the orographic effect with ISM circulation for precipitation in the Western Ghats[40], local instability to regional precipitation[41,42], and the ISM synoptic weather system (LPSs), especially across central to northern India[28,29]. Notable responses are also shown in south of eastern Himalayas in July and August, which are anticipated to be associated with westerly/southwesterly wind anomalies in the areas (Fig. 1d, e). Furthermore, extreme precipitation (see Methods for definition) exhibits similar patterns with some noticeable differences (Supplementary Fig. 2), demonstrating the necessity of exploring region-specific physical mechanisms at large to synoptic scales. Throughout a series of subsequent analyses, we focus on the regions of the (i) Western Ghats, (ii) south-central-east India, and (iii) Tamil Nadu, which exhibit greater climatological precipitation amounts (Supplementary Fig. 1) and distinct responses in RD-RU (Fig. 1b–g). Also, responses of precipitation in each area are expected to be primarily influenced by different physical mechanisms, as mentioned above. Our investigation excludes the northernmost part of India (north of the left box in Fig. 1b, c) and northeast India to focus on regions with the strongest precipitation changes and to avoid areas bordering Bangladesh.

For further analysis of the precipitation responses in individual regions, Fig. 2 shows the daily seasonal cycle of precipitation amounts over the Western Ghats (Fig. 2a), south-central-east India (Fig. 2b), and Tamil Nadu (Fig. 2c) during the selected 50-year periods under the CO_2 ramp-up and ramp-down phases. Consistent with Fig. 1, the Western Ghats and south-central-east India exhibit reductions in summer monsoon precipitation, particularly during June, July and mid-September to October (Fig. 2a, b). This leads to a delayed summer monsoon onset and earlier withdrawal during the CO_2 ramp-down period, resulting in a shortened duration of the summer monsoon by approximately 2 weeks compared with the CO_2 ramp-up period (Supplementary Fig. 3). Notably, daily precipitation differences between the two periods exhibit significant decreases with greater percentage values during the ISM onset periods (June, followed by July) than during its withdrawal periods (mid-September to October) (see the bottom panel of Fig. 2a, b). It should be emphasized that daily precipitation amounts are similar between the CO_2 ramp-up and ramp-down periods from August
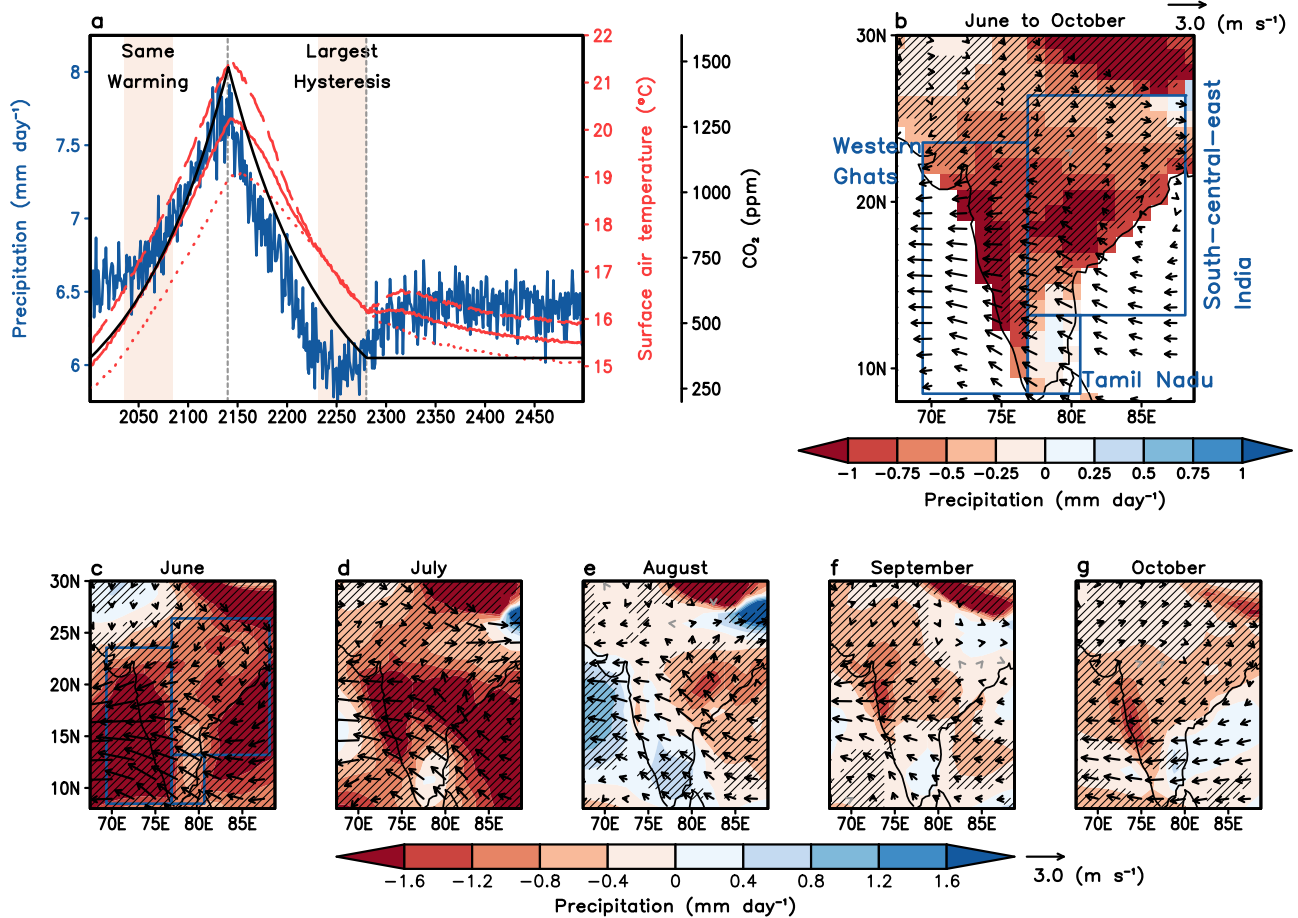
Fig. 1 | ISM precipitation responses to CDR. a Timeseries of forced atmospheric CO_2 concentration (black), simulated global (solid), NH (dashed), and SH (dotted) averaged annual mean surface air temperature (red), and ISM precipitation (blue; June to October averages; lands in 70–87.5°E, 8.5–26°N) in CESM1 28 ensemble simulation averages. Vertical gray dashed lines separate the CO_2 ramp-up, ramp-down and stabilization periods. The shading highlights the 50-year periods: (i) characterized by the largest hysteresis (negative overshoot) in ISM precipitation during CO_2 ramp-down period (years 2231–2280) and (ii) corresponding equivalent global warming levels appeared during CO_2 ramp-up phase (years 2035–2084). **b** Spatial pattern of the RD-RU precipitation (shading) and 850 hPa horizontal wind (vectors) averaged from June to October in CESM1 28 ensemble simulation averages. **c–g** Same as (**b**), but for (**c**) June, (**d**) July, (**e**) August, (**f**) September and

(**g**) October, including precipitation responses within ocean. **b–g** Black hatchings indicate regions with statistically significant precipitation differences at the 5% level based on a two-sided Student's t-test; vectors are shown in black where the zonal or meridional winds exhibit significant differences at the 5% level based on a two-sided Student's t-test, while colored gray when neither shows significant differences. **b, c** Blue boxes delineate Western Ghats (left box; since precipitation in that area is concentrated along the Western Ghats; lands within 70–76.875°E, 8.5–23.5°N), south-central-east India (right upper box; lands within 76.875–87.5°E, 13–26°N), and Tamil Nadu (right lower box; the southernmost state of India; lands within 76.875–80°E, 8.5–13°N) (only the lands within the boundaries are assigned to the individual regions).

to mid-September and late August to mid-September in the Western Ghats and south-central-east India, respectively. Tamil Nadu displays distinct precipitation responses compared to the other regions, with a weak but significant decrease from June to mid-July, followed by a significant increase from mid-July to August in RD-RU (Fig. 2c).

Changes in the daily precipitation intensity distribution (Fig. 2d–f) reveal coherent patterns. In the Western Ghats, a significant decrease is found in the frequency of light to heavy rainfall events in June and July, as well as from mid-September to October, with June exhibiting the most pronounced decrease compared to the other months (Fig. 2d). In contrast, the frequency of precipitation events exceeding 10 mm day^{-1} significantly increases from August to early September, along with a significant decrease in those weaker than ~5 mm day^{-1} and an increase in dry days (the lowest bin, represents no rainfall or rainfall events smaller than 1.0 mm day^{-1}; separately shown in Supplementary Fig. 4), respectively. This change in the daily precipitation intensity distribution suggests an increase in rainfall variability during the CO_2 ramp-down period when compared with the CO_2 ramp-up period, although the mean precipitation is similar between the two periods (Fig. 2a). South-central-east India likewise displays overall

significant decreases in the occurrence of precipitation events, particularly those with intensities greater than ~7 mm day^{-1} from June to early August, and those weaker than ~20 mm day^{-1} from late September to October (Fig. 2e). In contrast, from mid-August to mid-September, the region exhibits no prominent changes in daily precipitation intensity distribution. In both the Western Ghats and south-central-east India, all individual months show a significant increase in frequency of dry days (clearly shown in Supplementary Fig. 4), indicating a general weakening of the ISM. Tamil Nadu exhibits a significant shift in precipitation events from intensities greater than ~5 mm day^{-1} to weaker levels during June, while opposite changes are shown from mid-July to August (Fig. 2f), leading to weak, but significant precipitation decreases and increases in RD-RU, respectively (Fig. 2c).

Physical mechanisms for regional characteristics of hysteresis in ISM precipitation

From here, we explore the physical mechanisms underlying the distinct hysteresis in regional and subseasonal ISM precipitation under CDR. We investigate region-specific physical mechanisms across large to
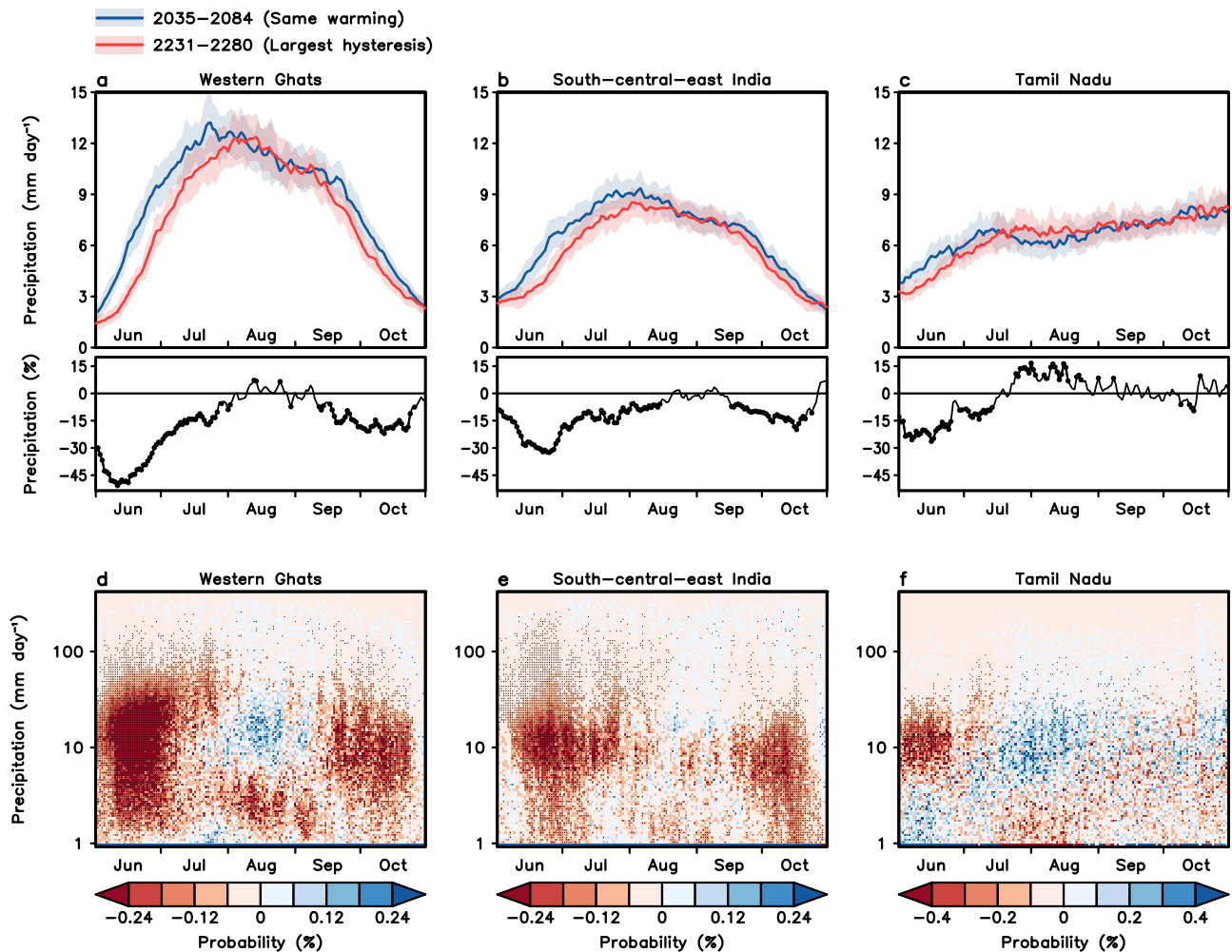
Fig. 2 | Hysteresis in regional and subseasonal ISM precipitation. a–c (above) Seasonal cycle of daily (June 1st to October 31st) precipitation climatology in **a** Western Ghats (lands within 70–76.875°E, 8.5–23.5°N), **b** south-central-east India (lands within 76.875–87.5°E, 13–26°N), and **c** Tamil Nadu (lands within 76.875–80°E, 8.5–13°N) during 50-year periods: (i) from years 2035 to 2084 (blue; equivalent global warming levels appeared during CO_2 ramp-up phase with years 2231–2280) and (ii) from years 2231 to 2280 (red; displaying the largest hysteresis (negative overshoot) in ISM precipitation during CO_2 ramp-down phase) from CESM1 28 ensemble simulation averages and ranges of plus-to-minus inter-ensemble standard deviations (shadings). (below) Percent anomalies of RD-RU precipitation, relative to the precipitation amount in CO_2 ramp-up period (years 2035–2084), calculated as $\frac{RD-RU\ precipitation}{Precipitation\ during\ CO_2\ ramp-up\ period} \times 100\%$. Black dots indicate the differences are statistically significant at 5% level based on a two-sided Student's t-test. Probabilistic differences of daily (from June 1st to October 31st) precipitation occurrence over **d** Western Ghats, **e** south-central-east India, and **f** Tamil Nadu in RD-RU with respect to precipitation intensities (y-axis; log-scale). Black dots indicate the differences are statistically significant at 5% level based on a two-sided Student's t-test.

synoptic scales. Specifically, we examine the role of large-scale thermodynamic drivers of ISM circulation, local thermodynamic stability, and ISM LPSs.

Monsoon circulation weakening induced by large-scale thermodynamic environmental changes

First, we investigate the role of the large-scale meridional temperature gradient in the middle to upper troposphere around India, which has been suggested to be the main large-scale thermodynamic driver of the ISM[43] (Methods). CESM1 is shown to well capture the observed relationship between the meridional temperature gradient and ISM precipitation (Supplementary Fig. 5). The zonal mean vertical profile of the RD-RU air temperature around India exhibits a reduced meridional temperature gradient surrounding the regions (Fig. 3a). Under the same global warming levels, the northern areas (5–35°N) display colder conditions than the southern areas (15°S to 5°N). The stronger recovery with a cooling trend in the NH can be attributed to the strong recovery over land under lower atmospheric CO_2 concentrations (Fig. 1a) and sustained weakening of the AMOC[13] during the selected 50-year period within the CO_2 ramp-down

phase compared to the CO_2 ramp-up phase. In addition, delayed recovery in the ocean (predominantly covering the SH), along with pronounced slow recovery in the Southern Ocean[14] could potentially contribute to the weakened meridional temperature gradient by damping the cooling trends (Fig. 3a).

Figure 3b shows that the meridional temperature gradient is positive from early June to mid-October during both the CO_2 ramp-up and ramp-down periods. However, the meridional temperature gradient decreases in the ramp-down period compared to the ramp-up period, shortening the length of the period with a positive temperature gradient. This change in the meridional temperature gradient is consistent with the reduction in monsoon duration in India (Supplementary Fig. 3). The diminished meridional temperature gradients (i.e., a negative large-scale thermodynamic indicator of the ISM) could weaken ISM circulation[22,23,27,43], possibly be associated with precipitation decreases across India. This is particularly evident in the Western Ghats, where the orographic effect, in conjunction with the ISM circulation, is a crucial rain-producing process[40]. Even though large-scale thermodynamic conditions contribute to the weakening of the ISM, these responses are observed throughout summer (Fig. 3b), suggesting that
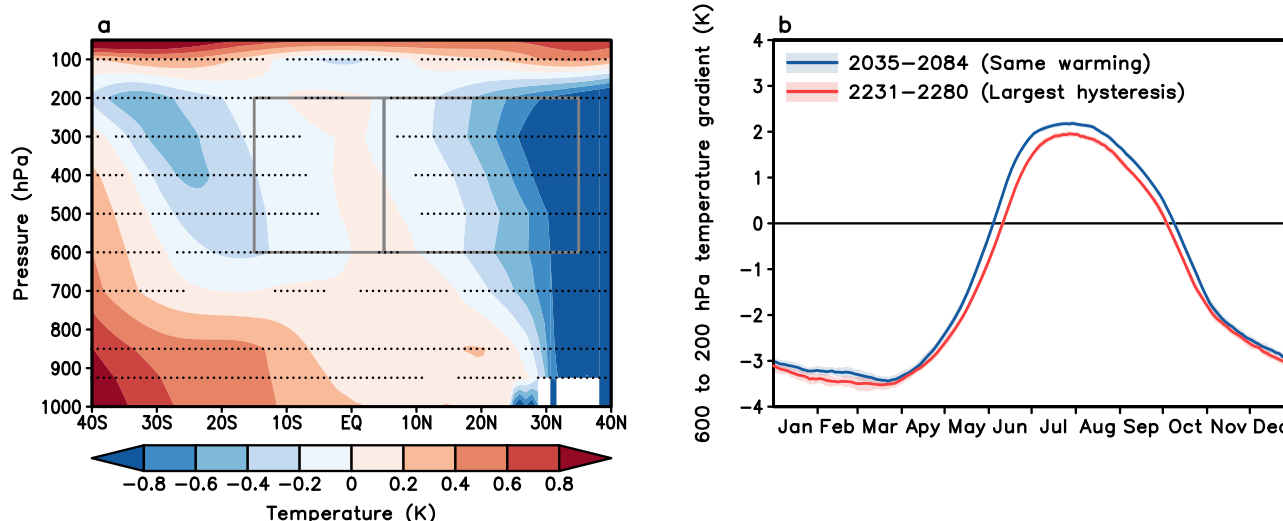
Fig. 3 | Hysteresis in large-scale thermodynamic conditions. a Zonal mean (40–100°E averages) vertical profile of air temperature responses in RD-RU during June to October averages from CESM1 28 ensemble simulation averages. Black stippling indicates regions with significant temperature changes in RD-RU at the 5% level based on a two-sided Student's *t*-test. **b** Seasonal cycle (from January 1st to December 31st) of daily middle to upper troposphere (600 to 200 hPa averages) meridional temperature gradient around India (40–100°E, northern (5–35°N) minus southern (15°S to 5°N) regions, illustrated as gray boxes in (**a**), respectively) during 50-year periods: (i) from years 2035 to 2084 (blue; equivalent global warming levels appeared during CO_2 ramp-up phase with years 2231–2280) and (ii) from years 2231 to 2280 (red; displaying the largest hysteresis (negative overshoot) in ISM precipitation during CO_2 ramp-down phase) from CESM1 28 ensemble simulation averages and ranges of plus-to-minus inter-ensemble standard deviations (shadings).

additional factors contribute to the distinct regional and subseasonal variations in the hysteresis of ISM precipitation.

Local thermodynamic stability changes

Second, we explore the influence of changes in local thermodynamic stability on the ISM precipitation hysteresis by employing deep convective inhibition (DCIN[44–46]; Methods), which is a measure of environmental thermodynamic stability for deep convection. Notably, the spatial pattern of DCIN differences in RD-RU (Fig. 4a–e) shows the strongest increase in June. In contrast, DCIN decreases appear over southern-to-central India, with meridional expansion or contraction varying month. The largest expansion toward higher latitudes appears in August and September. The DCIN patterns can primarily be attributed to changes in surface moist enthalpy (Supplementary Fig. 6). The DCIN decrease (i.e., lower stability) can counteract the effect of weakened monsoon circulation on precipitation across India. The combined influences of these factors lead to distinct regional and subseasonal precipitation responses in the RD-RU across India (Fig. 1c–g).

We analyze zonal mean responses of climate variables over India to understand the physical mechanisms driving the meridional expansion or contraction of DCIN increases in each month. A significant weakening of the monsoon precipitation occurs in June (Fig. 4f), which induces an increase in surface-reaching shortwave radiation[47,48] (Fig. 4g) and subsequent surface warming across India (Fig. 4h). Subsequently, the reduction in precipitation extends to higher latitudes (Fig. 4f), as the maximum climatological precipitation amounts appear at 17–19°N in July and August (Fig. 4k). In contrast, southern-to-central India exhibits specific humidity increases near the surface after late June (Fig. 4i) with enhanced surface latent heat flux (Fig. 4j), which is likely due to the surface warming and associated increase in potential evaporation. The surface warming and associated increase in specific humidity lead to the reduction in DCIN (Fig. 4b–e). The consistent latitudinal variations in surface specific humidity and DCIN reduction (compare Fig. 4a–e and i) also highlight the crucial role of surface humidification in driving the DCIN reduction. Even though surface exhibits distinct subseasonal responses within India (Fig. 4f–j), the meridional temperature gradient consistently decreases in the RD-RU during the summer (Fig. 3b), representing an independence between the responses in the context of subseasonal variations. Over the land, India experiences notable dry subsurface soil conditions in the RD-RU, especially during June and July, which become less severe in the subsequent months (Supplementary Fig. 7a–e). Nevertheless, substantial soil moisture exists in the subsurface during CO_2 ramp-down period (contours in Supplementary Fig. 7a–e). India shows an increase in surface evaporation from July to October, especially across southern-to-central India (Supplementary Fig. 7g–j), which is consistent with the rise in surface latent heat flux (Fig. 4j). Therefore, the changes in surface latent heat flux appear to be more strongly influenced by surface warming and associated increase in potential evaporation, rather than by drier land conditions.

ISM LPS changes

Lastly, we examine the response of ISM LPSs (Methods) in RD-RU, and its influence on the hysteresis of regional and subseasonal ISM precipitation. CESM1 realistically captures the genesis and track density of ISM LPSs (Fig. 5a–j) compared to those in the European Centre for Medium-Range Weather Forecasts reanalysis version 5 (ERA5)[49] data (Supplementary Fig. 8), although some biases are apparent (the potential role of the biases is discussed in the Summary and Conclusions section). We define LPS precipitation as the precipitation occurring around the center of the LPSs[28,30,35] (Methods; Supplementary Fig. 9 shows similar vortex-centered composite precipitation and atmospheric conditions maps between ERA5 and CESM1). Again, CESM1 realistically represents the contribution of LPSs to total and extreme precipitation (Fig. 5k–t) when compared to ERA5 (Supplementary Fig. 10), reinforcing the reliability of the results of the CESM1 simulations.

Owing to the pronounced weakening of the summer monsoon circulation across India in the RD-RU, there is a significant reduction in the genesis frequency of ISM LPSs throughout the ISM period, particularly around the northern/northwestern Bay of Bengal, where ISM LPSs primarily originate[35] (Fig. 6a–e; see climatology in Fig. 5a–e). The decrease in the genesis frequency of LPS across India and its surrounding regions (area-sum values are indicated in individual figures) is notably small during August, followed by September (Fig. 6c, d), possibly because the local stability decreases (Fig. 4c, d) and corresponding LPS genesis increases over the regions, including southern-to-central India.
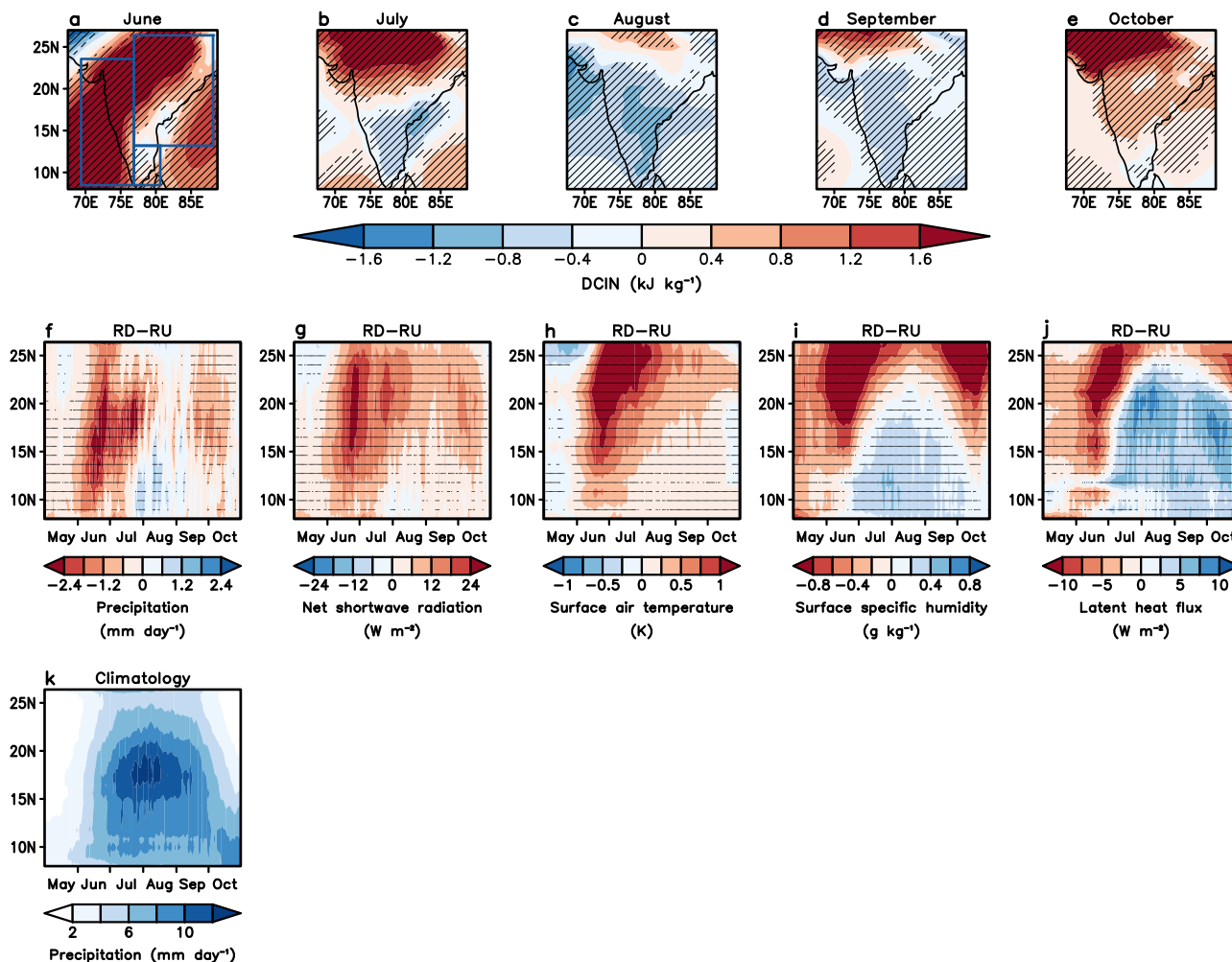
Fig. 4 | Responses in local thermodynamic stability. Spatial patterns of the RD-RU DCIN in **a** June, **b** July, **c** August, **d** September and **e** October. Black hatchings indicate regions with significant DCIN differences at the 5% level based on a two-sided Student's *t*-test. In (**a**), the blue boxes delineate the boundaries for Western Ghats (left box), south-central-east India (right upper box), and Tamil Nadu (right lower box) (only the lands within the boundaries are assigned to the individual regions). **f**–**j** Zonal (70–87.5°E) averaged daily (from May 1st to October 31st)

f precipitation, **g** net (downward minus upward; positive signs indicate from atmosphere to surface) shortwave radiation flux at surface, **h** surface air temperature, **i** surface specific humidity, and **j** latent heat flux (positive signs indicate from surface to atmosphere) responses in RD-RU from CESM1 28 ensemble simulation averages. Black dots indicate regions with significant differences at the 5% level based on a two-sided Student's *t*-test. **k** Climatology of zonal (70–87.5°E) averaged daily (from May 1st to October 31st) precipitation in CESM1 present-day simulation (Methods).

The track density of LPSs in the RD-RU exhibits a strong decline in and around the northwestern Bay of Bengal (Fig. 6f–j). However, in August and September, there are notable increases in LPS track density across western and southern-to-central India and the northeastern and central-to-eastern Arabian Sea (Fig. 6h, i). These increases are found to be associated with the increases in LPS genesis density around southern India (Supplementary Fig. 11). In addition, the tracks of LPSs that originated from the Bay of Bengal are shifted southwestward (e.g., Supplementary Fig. 11g). Together with the decreased DCIN in India, this southwestward shift in the LPS tracks aligns with the previously suggested LPS propagation mechanisms[30,38], where diabatic heating shifts the LPS westward/southwestward through non-linear self-advection processes. Furthermore, the average lifetime of LPSs exhibits increases in August during RD-RU (Supplementary Fig. 12a), possibly because of the decrease in DCIN within India. Moreover, with operation of the physical processes under the decreased DCIN, LPSs exhibit a tendency to propagate zonally faster in RD-RU during both August and September (Supplementary Fig. 12b). In addition, the changes in the LPS track density may bolster the increase in surface humidity within southern-to-central India, as LPSs typically accompany high levels of atmospheric humidity (Supplementary Fig. 13), establishing a positive feedback loop between them. These responses contribute to the increased track density within

southern-to-central India and the northeastern and central-to-eastern Arabian Sea during August and September (Fig. 6h, i). The resulting alterations in the track density of the LPSs contribute to the distinct hysteresis in regional and subseasonal ISM precipitation.

Responses of LPS precipitation and non-LPS precipitation exhibit distinct spatial distributions (Fig. 7). The changes in precipitation associated with the LPSs (Fig. 7a–e) closely resemble the LPS track density changes (Fig. 6f–j). South-central-east India exhibits significant decreases in LPS precipitation in all individual months. In contrast, LPS precipitation increases are shown in the Western Ghats in August, and in the southernmost India in August and September. Conversely, non-LPS precipitation demonstrates two notable features: strong reduction in the Western Ghats in all individual months, and weak increases or insignificant changes in Tamil Nadu from July to October (Fig. 7f–j). Non-LPS precipitation generally exhibits decreases in south-central-east India, although the responses are much smaller than the LPS-induced changes (Fig. 7).

The results depicted in Fig. 7 suggest that the decrease in precipitation appearing in the Western Ghats (Fig. 1c–g) can be mainly attributed to the reduction in non-LPS precipitation associated with the weakening of ISM circulation. Changes in LPS-associated precipitation further reduce precipitation in June, July, and October, but they offset the precipitation
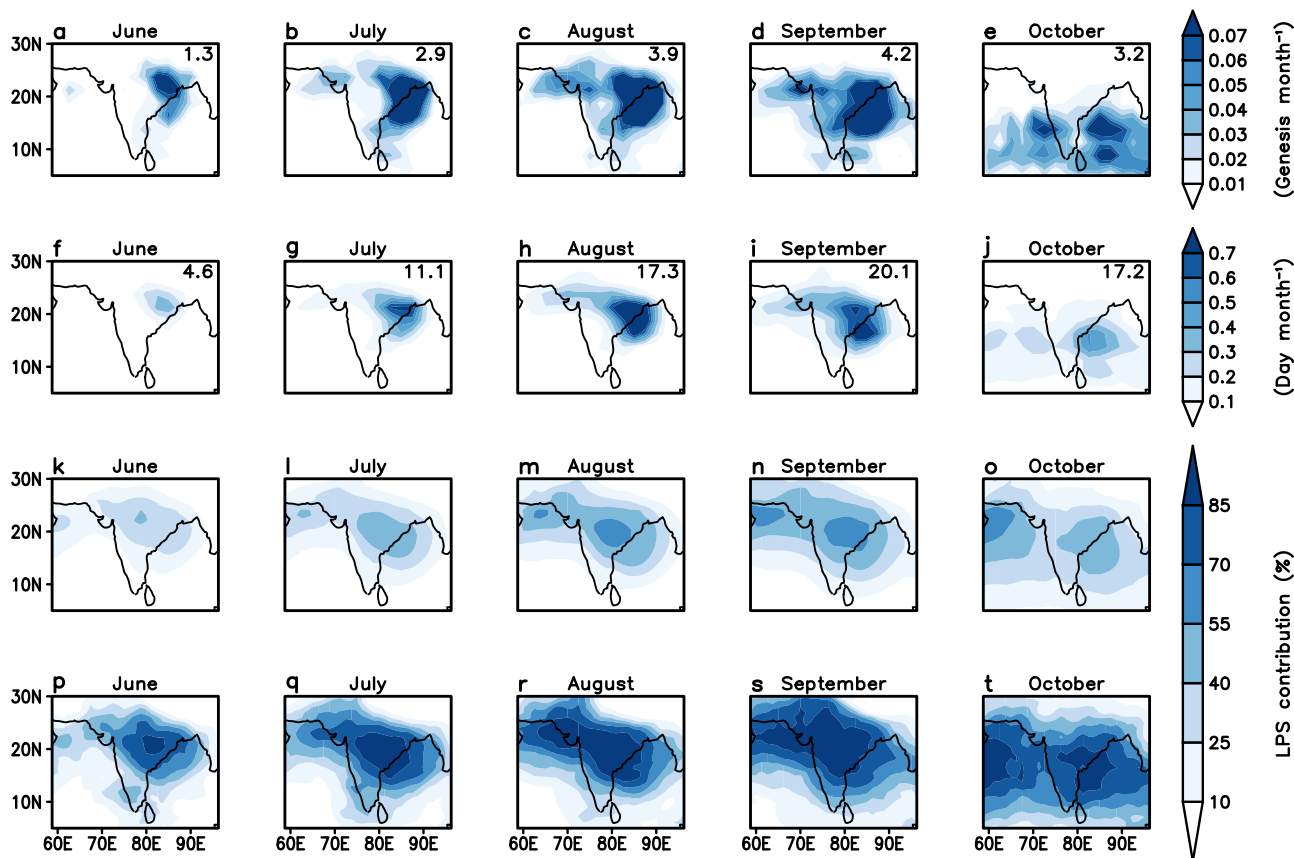
Fig. 5 | Evaluation of the representation of LPSs and LPS-induced precipitation across India in CESM1. Spatial patterns of the climatology for ISM LPS (**a–e**) genesis, (**f–j**) track density (i.e., frequency), ISM LPS contribution to (**k–o**) total precipitation, and (**p–t**) extreme precipitation amount from CESM1 28 ensemble simulations (from the initial 10-year, 2001–2010) for individual months (June, July, August, September, and October from left to right columns). **a–j** To enhance visibility, results are presented with 2.5° × 2.5° resolution, and the sum of values within the region of 60–95°E, 5–30°N is presented in the upper-right corner of each figure. **k–t** A rain event is considered LPS-driven, when it occurs within an 8° radius of an LPS center[28,30,35]. Here, extreme precipitation is defined as the 99th percentile 6-hourly precipitation amount for individual months and respective grids, from CESM1 28 ensemble simulations (280 years from initial 10 years of the 28 ensembles).

decreases in August. In September, LPS precipitation decreases and increases across the northern and southern Western Ghats, respectively, corresponding to a shift in LPS tracks during this period (Fig. 6i). These results are reasonable, as changes in LPSs may influence precipitation in the Western Ghats by affecting the orographic effect through wind anomalies[50,51]. The decrease in precipitation shown in south-central-east India during all individual months (Fig. 1c–g) is predominantly attributable to reduced LPS precipitation (Fig. 7).

In Tamil Nadu, the decrease in precipitation during June is due to the weakening of the ISM, while the insignificant or weak increase in precipitation from July to October is a result of the DCIN decrease-induced non-LPS precipitation increases (Fig. 7f–j, in comparison with Fig. 1c–g). Additionally, during August and September, the southernmost India exhibits a weak increase in LPS-associated precipitation (Fig. 7c, d), aligned with LPS track density changes (Fig. 6h, i).

We extend our examination to the hysteresis of extreme precipitation (see Methods for definitions) originating from LPS or non-LPS events across India (Fig. 8). The hysteresis of LPS significantly contributes to the hysteresis of the total extreme precipitation amounts in RD-RU, notably to a greater extent than non-LPS associated changes (Fig. 8). The hysteresis of LPS-associated extreme precipitation (Fig. 8a–e) generally exhibits spatial structures consistent with the total precipitation responses (Fig. 7a–e), which are also aligned with the hysteresis of LPS trajectories (Fig. 6f–j). Specifically, strong decreases are shown in south-central-east India during all individual months and in the central-to-northern/northern parts of the Western Ghats, except for August. Notable increases in extreme

precipitation induced by LPS events appear in the Western Ghats during August (Fig. 8c), consistent with the patterns shown in the total precipitation changes (Fig. 7c). Furthermore, extreme precipitation amounts unrelated to LPSs exhibit a decrease in the Western Ghats, particularly pronounced in June, and are attributed to ISM circulation weakening, while intensities are reduced in subsequent months (Fig. 8f–j). In addition, increases in LPS and non-LPS extreme precipitation are shown in south of central/eastern Himalayas in July and August (Fig. 8b, c, g, h). The increases in non-LPS extreme precipitation are aligned with total precipitation responses (Figs. 1d, e and 7g, h), which can be attributed to westerly/ southwesterly 850 hPa wind anomalies in the areas from enhanced meridional temperature gradient with most pronounced warming within the India in July and August (Supplementary Fig. 14, Fig. 4h). The LPS-induced extreme precipitation increases are aligned with enhanced LPS track density over the regions (Fig. 6g, h), can be attributed to the westerly wind anomalies (Supplementary Fig. 14a, b), along with decayed positive DCIN in August (Fig. 4c).

Discussion

The objective of this study is to examine the regional and subseasonal characteristics of the ISM precipitation changes under an idealized CDR scenario. Our approach differs from that of prior studies[22–24,27] as we specifically focus on regional features and analyze subseasonal/high-frequency precipitation variability. We explain the spatiotemporally heterogeneous hysteresis in the ISM precipitation response with changes in three main factors: ISM circulation, local thermodynamic stability and ISM LPS.
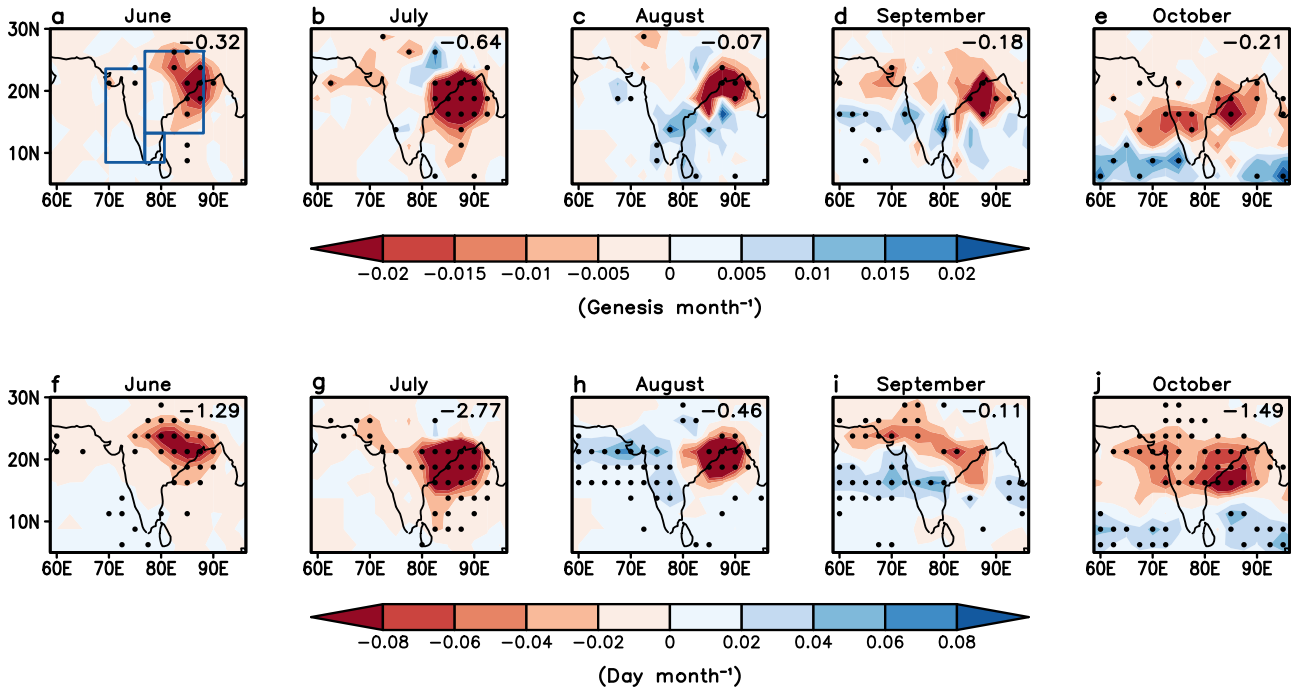
Fig. 6 | Hysteresis in ISM LPSs. Spatial patterns of the RD-RU **a–e** genesis frequency, **f–j** track density of ISM LPSs in **a, f** June, **b, g** July, **c, h** August, **d, i** September and **e, j** October from CESM1 28 ensemble simulation averages. The sum of values within the region of 60–95°E, 5–30°N is presented in the upper-right corner of each figure. Black dots indicate regions with statistically significant differences at the 5% level based on a two-sided Student's *t*-test. To enhance visibility, results are presented with 2.5° × 2.5° resolution. In **a**, the blue boxes delineate the boundaries for Western Ghats (left box), south-central-east India (right upper box), and Tamil Nadu (right lower box) (only the lands within the boundaries are assigned to the individual regions).
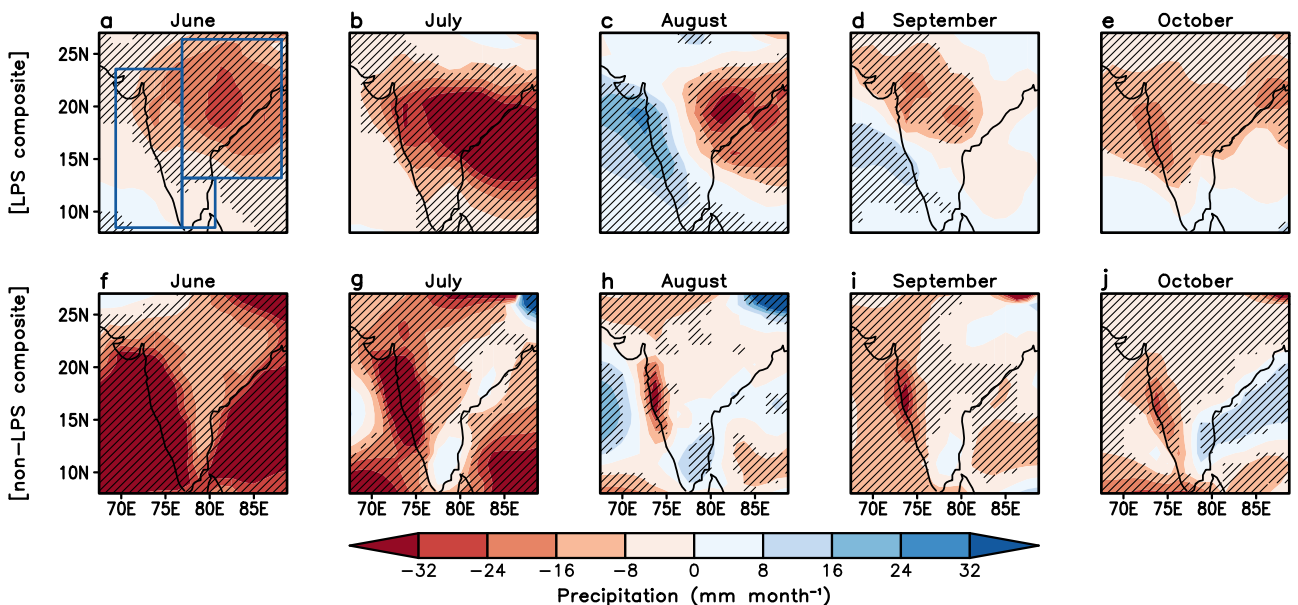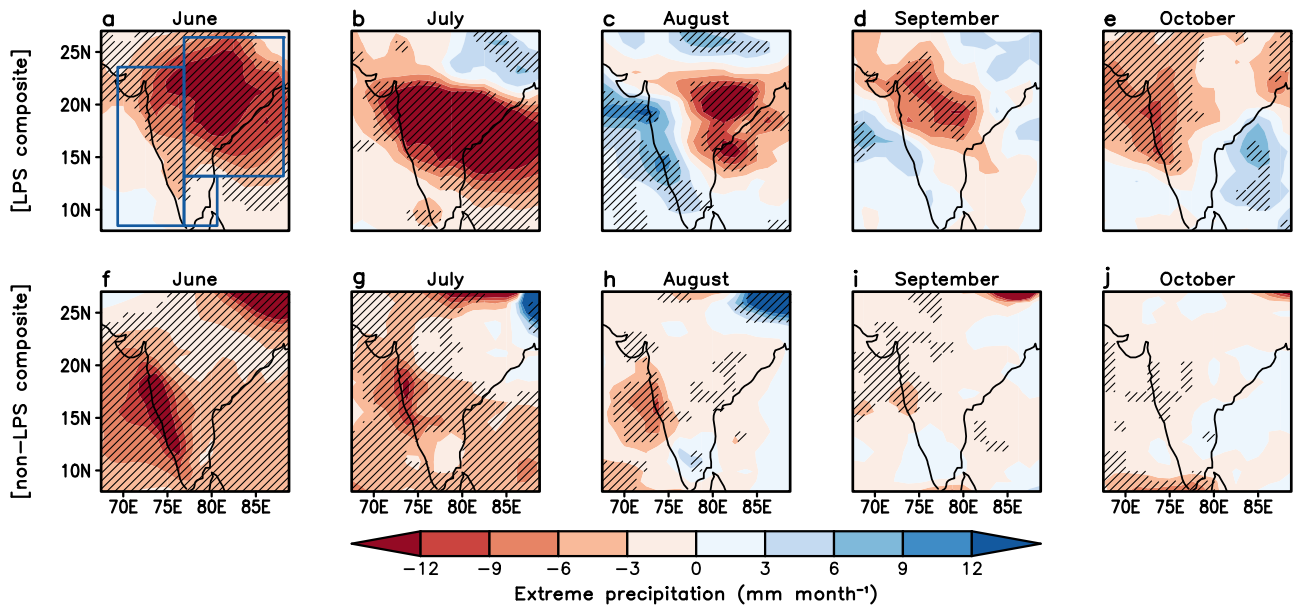

Fig. 7 | Hysteresis of LPS and non-LPS originated precipitation. Spatial patterns of the RD-RU **a–e** LPS-induced, **f–j** non-LPS-induced total precipitation amounts during **a, f** June, **b, g** July, **c, h** August, **d, i** September and **e, j** October from CESM1 28 ensemble simulation averages. Black hatchings indicate regions with statistically significant differences at the 5% level based on a two-sided Student's *t*-test. In **a**, the blue boxes delineate the boundaries for Western Ghats (left box), south-central-east India (right upper box), and Tamil Nadu (right lower box) (only the lands within the boundaries are assigned to the individual regions).

The ISM seasonal mean precipitation exhibits a negative over-shoot during the CO_2 ramp-down period, as previously suggested[22,23,27], but features spatially and temporally inhomogeneous responses. Generally, the precipitation reductions in RD-RU are more pronounced in June and July than in August–October. In RD-RU, the Western Ghats and south-central-east India commonly exhibit precipitation decreases during June, July and mid-September to October, leading to a shortened ISM duration of approximately 2 weeks. In contrast, the difference in the RD-RU precipitation is small between August and mid-September. Tamil Nadu exhibits distinct precipitation responses, characterized by decreases from June to mid-July and increases from mid-July to August.

Fig. 8 | Hysteresis of LPS and non-LPS originated extreme precipitation. Spatial patterns of the RD-RU **a**–**e** LPS, **f**–**j** non-LPS induced total extreme precipitation amounts during **a**, **e** June, **b**, **g** July, **c**, **h** August, **d**, **i** September and **e**, **j** October from CESM1 28 ensemble simulation averages. Black hatchings indicate regions with statistically significant differences at the 5% level based on a two-sided Student's *t*-test. In **a**, the blue boxes delineate the boundaries for Western Ghats (left box), south-central-east India (right upper box), and Tamil Nadu (right lower box) (only the lands within the boundaries are assigned to the individual regions).

We show that the spatially and temporally complex precipitation responses in the RD-RU originated from three major sources: (i) ISM circulation, (ii) local thermodynamic stability, and (iii) ISM LPSs. ISM circulation is weakened, which could be related to a reduced meridional temperature gradient around India. Following this initial weakening, local thermodynamic stability decreases, particularly in August and September, driven by surface warming and increased surface specific humidity. LPS genesis becomes less frequent across India and its surrounding regions, but increases notably in the southern-to-central Bay of Bengal, southern India, and northeastern Arabian Sea during August, and over southern India and the central-to-eastern Arabian Sea during September. As a result, LPS track density increases in western and southern-to-central India during the August and September, due to increased LPS genesis, which can be attributed to decreased thermodynamic stability (reductions in DCIN). Our results indicate that the reduced precipitation in the Western Ghats is primarily due to weakened ISM circulation, with additional reduction from the reduced LPS track density in its central-to-northern areas. The decrease in local thermodynamic stability counteracts the weakening of the monsoon circulation in its southernmost regions, resulting in a weak decrease or even increase in precipitation from July to October. In addition, in August and to a lesser extent in September, LPS propagates more frequently down to the Western Ghats in the RD-RU, leading to insignificant/increased precipitation. In contrast, precipitation decreases over south-central-east India, which is mostly associated with a decrease in LPS track density. Insignificant or increased precipitation over Tamil Nadu in RD-RU can be understood as a result of the competition between ISM circulation weakening and local stability decreasing with an additional increase in precipitation from LPS-precipitation. Supplementary Fig. 15 summarizes the sources of hysteresis in the total precipitation contributions from LPS- or non-LPS-induced changes, with the suggested distinct spatial patterns that vary across individual months.

A similar spatial pattern is shown in the hysteresis of extreme precipitation, which are more strongly influenced by changes in ISM LPSs. These findings indicate the importance of comprehending the responses of synoptic weather systems, such as ISM LPSs, to CDR, as they can have a critical impact on the hysteresis of the hydroclimate over India, particularly affecting extreme rainfall events.

Limitations possibly remain in our analysis, originating from the imperfect representation of ISM LPSs in the CESM1 simulations. This includes a low bias in the frequency of LPS genesis in June and a slightly southward arrangement of LPSs compared to ERA5 (in comparison to Fig. 5a–j and Supplementary Fig. 8), aligned with a prior study[52]. However, these biases are not expected to qualitatively affect our conclusions because LPSs do not play a decisive role in shaping the spatial patterns of precipitation responses in June. In addition, the broad area of LPS changes in August and September, and the inherently wide diameter of LPSs, typically around 1000 km, further support the insensitivity of our results. Additionally, the relatively coarser horizontal resolution (~1°) employed in our model simulations is not anticipated to be problematic, as we adopted an appropriate methodology for LPS detection, which has been suggested to generally not rely on horizontal resolution of the datasets[36].

Our results reveal distinct hysteresis characteristics in regional and subseasonal ISM precipitation, arising from counteracting effects that follow the initial weakening stage of monsoon circulation in the CESM1 multi-ensemble simulations. These model simulation datasets provide a valuable opportunity for this study, as they allow for the analysis of the influence of 6-hourly and synoptic weather systems, which have a crucial influence on regional and subseasonal ISM precipitation changes in response to CDR. Furthermore, the utilization of a multi-ensemble analysis approach is particularly valuable for this study because it enables us to discern clear signals that extend beyond the significant impacts of internal variability in the analysis of weather systems in a specific region. Nevertheless, caveats may arise from reliance on a single climate model. To address this concern, we conducted a parallel analysis using CMIP6 CDRMIP multi-model simulations[25,53], each with one ensemble, and obtained similar results (Supplementary Fig. 16), demonstrating the robustness of our findings. Nevertheless, the CMIP6 CDRMIP multi-model simulation averages exhibited relatively uneven results (Supplementary Fig. 16c–e), highlighting the advantages of using multi-ensemble simulations in the analysis.

Conducting additional multi-ensemble simulations that incorporate a diverse array of climate models is crucial for a more specific evaluation of the changes and associated uncertainties in hydroclimates at regional and shorter-term scales. This approach can enhance our understanding of the impact of synoptic-scale weather system responses to various CO_2 pathways, including CDR, and the achievement of net-zero CO_2 emissions[54].

When conducting analyses in this context, it is essential to consider various emission trajectories[55]. Furthermore, there is a need to understand climate responses in an equilibrium climate state that extends beyond transient CO_2 pathways[56,57]. This broader perspective is crucial for gaining insight into the long-term implications and dynamics of climate change.

Methods

Model simulation experimental design

We employed idealized CO_2 pathway simulations conducted using the Community Earth System Model version 1.2.2 (CESM1)[39], which have been widely utilized in recent studies to investigate climate responses to CDR across various aspects, including the AMOC, ENSO and monsoons[13,17,22,27]. The atmospheric component (Community Atmospheric Model version 5, CAM5)[58], employed a horizontal resolution of ~0.94° latitude ×1.25° longitude with 30 vertical levels. It was coupled with the Parallel Ocean Program version 2 (POP2)[59], Community Land Model version 4 (CLM4)[60,61], and Community Ice Code version 4 (CICE4)[62]. The land model incorporates the carbon-nitrogen cycle.

A fixed CO_2 concentration (367 ppm) simulation of CESM1 was conducted for 900 years (present-day simulation). Subsequently, 28 ensemble simulations were performed with varied initial conditions, featuring a 1% annual increase in the CO_2 concentration over 140 years (years 2001–2140), reaching a quadrupled level (1468 ppm). This was followed by a symmetrical CO_2 concentration decrease (minus 1% per year) over the subsequent 140 years (years 2141–2280), returning the CO_2 concentration to the initial level of 367 ppm. The subsequent years were simulated using a constant CO_2 concentration of 367 ppm. Detailed analyses were conducted for specific 50-year periods, emphasizing maximal hysteresis in ISM precipitation during the CO_2 ramp-down period (years 2231–2280), with a comparative assessment of another 50-year period during the CO_2 ramp-up phase (years 2035–2084), featuring the same global warming levels. The discrepancies between the two periods are denoted as RD-RU (2231–2280 subtracted by 2035–2084).

Extreme precipitation

For CESM1, the threshold of extreme precipitation was defined as the 99th percentile of the 6-hourly precipitation in each individual month and grid location from the present-day simulation.

Large-scale thermodynamic indicator of Indian summer monsoon precipitation

A large-scale thermodynamic index[43] for the Indian summer monsoon (ISM) precipitation was employed. This index relies on a large-scale meridional temperature gradient around India, specifically the difference in middle to upper tropospheric (averaged from 600 to 200 hPa) temperatures between the northern (40–100°E, 5–35°N) and southern (40–100°E, 15°S to 5°N) regions. This gradient serves as a significant indicator of the onset, withdrawal and rainfall amounts of the ISM by establishing an off-equatorial large-scale deep heat source[43].

Local thermodynamic stability

Throughout summer, intense rainfall events across India are strongly linked to local deep convective inhibition[41,42] (DCIN)[44–46], often represented by a vertical gradient of moist enthalpy (h). In this study, DCIN was quantified as the disparity between the saturation moist enthalpy (h^*) at 700 hPa and the surface h, expressed as follows:

$$h = C_p T + L_v q,$$

$$DCIN = h^*_{700hPa} - h_{surface},$$

where C_p is the specific heat capacity of dry air at constant pressure, T is the temperature, L_v is the latent heat of vaporization, and q is the specific humidity. For an undiluted parcel launched near the surface, the resulting DCIN thermodynamically measures the degree to which the rising parcel is less buoyant than the surrounding environment in the lower troposphere.

ISM low-pressure system tracking algorithm and precipitation

We employed a validated tracking algorithm[35] developed for ISM low-pressure systems (LPSs), which is grounded on the TempestExtremes framework[63,64]. This approach involves searching for minima in the 850 hPa horizontal wind streamfunction field, necessitating an increase of 12.5×10^5 $m^2\ s^{-1}$ from the central minimum within a 10° radius to identify vortices. Candidates are linked based on various criteria, including (1) a maximum distance of 3.0° between in-sequence candidates, (2) a minimum length of 5 time points in 6-hourly data (i.e., ensure track lasts longer than 1 day), (3) a maximum time interval of in-sequence candidates as 12 h, (4) surface geopotential less than 8000 $m^2\ s^{-2}$ for at least four 6-hourly time steps along the track, and (5) 850 hPa relative humidity higher than 85% for at least four 6-hourly time steps along the track[35].

The estimated LPSs are linked to precipitation events when rainfall occurs within an 8° radius of an LPS center within a 6-h timeframe, as in previous studies[28,30,35].

Data availability

CESM1 simulation datasets supporting the results will be provided upon a reasonable request. Global Precipitation Climatology Project version 2.3 can be accessed at https://www.ncei.noaa.gov/data/global-precipitation-climatology-project-gpcp-monthly/access/. ERA5 datasets can be accessed at https://doi.org/10.24381/cds.bd0915c6, https://doi.org/10.24381/cds.adbb2d47 and https://doi.org/10.24381/cds.6860a573. Global Precipitation Climatology Centre version 2022 can be accessed at https://opendata.dwd.de/climate_environment/GPCC/html/fulldata-monthly_v2022_doi_download.html. All of the CMIP6 model simulation datasets used in this study can be accessed at https://esgf-node.llnl.gov/search/cmip6/.

Code availability

The code used in this study will be provided upon a reasonable request.

References

1. IPCC *Climate Change 2021*: *The Physical Science Basis. Contribution of Working Group I to the Sixth Assessment Report of the Intergovernmental Panel on Climate Change* (eds. Masson-Delmotte, V. et al.) (Cambridge University Press, 2021).
2. Allen, M. R. & Ingram, W. J. Constraints on future changes in climate and the hydrologic cycle. *Nature* **419**, 224–232 (2002).
3. Zhang, X. et al. Detection of human influence on twentieth-century precipitation trends. *Nature* **448**, 461–465 (2007).
4. Min, S.-K., Zhang, X., Zwiers, F. W. & Hegerl, G. C. Human contribution to more-intense precipitation extremes. *Nature* **470**, 378–381 (2011).
5. Paik, S. et al. Determining the anthropogenic greenhouse gas contribution to the observed intensification of extreme precipitation. *Geophys. Res. Lett.* **47**, e2019GL086875 (2020).
6. Lee, J.-Y. et al. Future global climate: scenario-based projections and near-term information. In *Climate Change 2021: The Physical Science Basis. Contribution of Working Group I to the Sixth Assessment Report of the Intergovernmental Panel on Climate Change* (eds. Masson-Delmotte, V. et al.) 553–672 (Cambridge University Press, 2021).
7. Paik, S., An, S.-I., Min, S.-K., King, A. D. & Kim, S.-K. Emergent constraints on future extreme precipitation intensification: from global to continental scales. *Weather Clim. Extrem.* **42**, 100613 (2023).
8. Liu, Z., Deng, Z., Davis, S. J. & Ciais, P. Global carbon emissions in 2023. *Nat. Rev. Earth Environ.* **5**, 253–254 (2024).

9. UNFCCC *Adoption of the Paris Agreement*, http://unfccc.int/resource/docs/2015/cop21/eng/l09r01.pdf (2015).

10. Kim, S.-K. et al. Widespread irreversible changes in surface temperature and precipitation in response to CO_2 forcing. *Nat. Clim. Chang.* **12**, 834–840 (2022).

11. Boucher, O. et al. Reversibility in an Earth System model in response to CO_2 concentration changes. *Environ. Res. Lett.* **7**, 024013 (2012).

12. Wu, P., Ridley, J., Pardaens, A., Levine, R. & Lowe, J. The reversibility of CO_2 induced climate change. *Clim. Dyn.* **45**, 745–754 (2015).

13. An, S.-I. et al. Global cooling hiatus driven by an AMOC overshoot in a carbon dioxide removal scenario. *Earths Future* **9**, e2021EF002165 (2021).

14. Kug, J.-S. et al. Hysteresis of the intertropical convergence zone to CO_2 forcing. *Nat. Clim. Chang.* **12**, 47–53 (2022).

15. Song, S.-Y. et al. Asymmetrical response of summer rainfall in East Asia to CO_2 forcing. *Sci. Bull.* **67**, 213–222 (2022).

16. Kim, S.-Y. et al. Hemispherically asymmetric Hadley cell response to CO_2 removal. *Sci. Adv.* **9**, eadg1801 (2023).

17. Liu, C. et al. Hysteresis of the El Niño-Southern Oscillation to CO_2 forcing. *Sci. Adv.* **9**, eadh8442 (2023).

18. Oh, J.-H. et al. Emergent climate change patterns originating from deep ocean warming in climate mitigation scenarios. *Nat. Clim. Chang.* **14**, 260–266 (2024).

19. Wu, P., Wood, R., Ridley, J. & Lowe, J. Temporary acceleration of the hydrological cycle in response to a CO_2 rampdown. *Geophys. Res. Lett.* **37**, L12705 (2010).

20. Yeh, S.-W., Song, S.-Y., Allan, R. P., An, S.-I. & Shin, J. Contrasting response of hydrological cycle over land and ocean to a changing CO_2 pathway. *npj Clim. Atmos. Sci.* **4**, 53 (2021).

21. Mondal, S. K. et al. Hysteresis and irreversibility of global extreme precipitation to anthropogenic CO_2 emission. *Weather Clim. Extrem.* **40**, 100561 (2023).

22. Oh, H. et al. Contrasting hysteresis behaviors of Northern Hemisphere land monsoon precipitation to CO_2 pathways. *Earths Future* **10**, e2021EF002623 (2022).

23. Zhang, S., Qu, X., Huang, G. & Hu, P. Asymmetric response of South Asian summer monsoon rainfall in a carbon dioxide removal scenario. *npj Clim. Atmos. Sci.* **6**, 10 (2023).

24. Zhang, S. et al. Delayed onset of Indian summer monsoon in response to CO_2 removal. *Earths Future* **12**, e2023EF004039 (2024).

25. Keller, D. P. et al. The Carbon Dioxide Removal Model Intercomparison Project (CDRMIP): rationale and experimental protocol for CMIP6. *Geosci. Model Dev.* **11**, 1133–1160 (2018).

26. Jo, S.-Y. et al. Hysteresis behaviors in East Asian extreme precipitation frequency to CO_2 pathway. *Geophys. Res. Lett.* **49**, e2022GL099814 (2022).

27. Paik, S., An, S.-I., Min, S.-K., King, A. D. & Shin, J. Hysteretic behavior of global to regional monsoon area under CO_2 ramp-up and ramp-down. *Earths Future* **11**, e2022EF003434 (2023).

28. Hunt, K. M. R. & Fletcher, J. K. The relationship between Indian monsoon rainfall and low-pressure systems. *Clim. Dyn.* **53**, 1859–1871 (2019).

29. Thomas, T. M., Bala, G. & Srinivas, V. V. Characteristics of the monsoon low pressure systems in the Indian subcontinent and the associated extreme precipitation events. *Clim. Dyn.* **56**, 1859–1878 (2021).

30. Vishnu, S., Risser, M. D., O'Brien, T. A., Ullrich, P. A. & Boos, W. R. Observed increase in the peak rain rates of monsoon depressions. *npj Clim. Atmos. Sci.* **6**, 111 (2023).

31. Dash, S. K., Jenamani, R. K., Kalsi, S. R. & Panda, S. K. Some evidence of climate change in twentieth-century India. *Clim. Change* **85**, 299–321 (2007).

32. Cohen, N. Y. & Boos, W. R. Has the number of Indian summer monsoon depressions decreased over the last 30 years? *Geophys. Res. Lett.* **41**, 7846–7853 (2014).

33. Sandeep, S., Ajayamohan, R. S., Boos, W. R., Sabin, T. P. & Praveen, V. Decline and poleward shift in Indian summer monsoon synoptic activity in a warming climate. *Proc. Natl Acad. Sci. USA* **115**, 2681–2686 (2018).

34. Vishnu, S., Francis, P. A., Shenoi, S. S. C. & Ramakrishna, S. S. V. S. On the decreasing trend of the number of monsoon depressions in the Bay of Bengal. *Environ. Res. Lett.* **11**, 014011 (2016).

35. Vishnu, S., Boos, W. R., Ullrich, P. A. & O'Brien, T. A. Assessing historical variability of South Asian monsoon lows and depressions with an optimized tracking algorithm. *J. Geophys. Res. Atmos.* **125**, e2020JD032977 (2020).

36. Vishnu, S., Boos, W. R. & Collins, W. D. Historical and future trends in South Asian monsoon low pressure systems in a high-resolution model ensemble. *npj Clim. Atmos. Sci.* **6**, 182 (2023).

37. Dong, W., Ming, Y. & Ramaswamy, V. Projected changes in South Asian monsoon low pressure systems. *J. Clim.* **33**, 7275–7287 (2020).

38. You, Y. & Ting, M. Observed trends in the South Asian monsoon low-pressure systems and rainfall extremes since the late 1970s. *Geophys. Res. Lett.* **48**, e2021GL092378 (2021).

39. Hurrell, J. W. et al. The Community Earth System Model: a framework for collaborative research. *Bull. Am. Meteorol. Soc.* **94**, 1339–1360 (2013).

40. Tawde, S. A. & Singh, C. Investigation of orographic features influencing spatial distribution of rainfall over the Western Ghats of India using satellite data. *Int. J. Climatol.* **35**, 2280–2293 (2015).

41. Pattanaik, D. R. & Rajeevan, M. Variability of extreme rainfall events over India during southwest monsoon season. *Meteorol. Appl.* **17**, 88–104 (2010).

42. Bajrang, C., Attada, R. & Goswami, B. N. Possible factors for the recent changes in frequency of central Indian Summer Monsoon precipitation extremes during 2005–2020. *npj Clim. Atmos. Sci.* **6**, 120 (2023).

43. Xavier, P. K., Marzin, C. & Goswami, B. N. An objective definition of the Indian summer monsoon season and a new perspective on the ENSO-monsoon relationship. *Q. J. R. Meteorol. Soc.* **133**, 749–764 (2007).

44. Raymond, D. J. et al. Convective forcing in the intertropical convergence zone of the eastern Pacific. *J. Atmos. Sci.* **60**, 2064–2082 (2003).

45. Fuchs, Ž., Sessions, S. L. & Raymond, D. J. Mechanisms controlling the onset of simulated convectively coupled Kelvin waves. *Tellus A Dyn. Meteorol. Oceanogr.* **66**, 22107 (2014).

46. Weber, N. J., Kim, D. & Mass, C. F. Convection-Kelvin wave coupling in a global convection-permitting model. *J. Atmos. Sci.* **78**, 1039–1055 (2021).

47. Rajeevan, M. & Srinivasan, J. Net cloud radiative forcing at the top of the atmosphere in the Asian monsoon region. *J. Clim.* **13**, 650–657 (2000).

48. Johansson, E., Devasthale, A., L'Ecuyer, T., Ekman, A. M. L. & Tjernström, M. The vertical structure of cloud radiative heating over the Indian subcontinent during summer monsoon. *Atmos. Chem. Phys.* **15**, 11557–11570 (2015).

49. Hersbach, H. et al. The ERA5 global reanalysis. *R. Meteorol. Soc.* **146**, 1999–2049 (2020).

50. Krishnamurthy, V. & Ajayamohan, R. S. Composite structure of monsoon low pressure systems and its relation to Indian rainfall. *J. Clim.* **23**, 4285–4305 (2010).

51. Hunt, K. M. R. et al. Modes of coastal precipitation over southwest India and their relationship with intraseasonal variability. *Q. J. R. Meteorol. Soc.* **147**, 181–201 (2021).

52. Thomas, T. M., Bala, G. & Vemavarapu, S. V. CESM simulation of monsoon low pressure systems over India. *Int. J. Climatol.* **42**, 5964–5984 (2022).

53. Eyring, V. et al. Overview of the Coupled Model Intercomparison Project Phase 6 (CMIP6) experimental design and organization. *Geosci. Model Dev.* **9**, 1937–1958 (2016).

54. King, A. D. et al. Preparing for a post-net-zero world. *Nat. Clim. Chang.* **12**, 775–777 (2022).

55. Meinshausen, M. et al. A perspective on the next generation of Earth system model scenarios: towards representative emission pathways (REPs). *Geosci. Model Dev.* **17**, 4533–4559 (2024).

56. King, A. D., Lane, T. P., Henley, B. J. & Brown, J. R. Global and regional impacts differ between transient and equilibrium warmer worlds. *Nat. Clim. Chang.* **10**, 42–47 (2020).

57. King, A. D. et al. Transient and quasi-equilibrium climate states at 1.5°C and 2°C global warming. *Earths. Future* **9**, e2021EF002274 (2021).

58. Neale, R. B. et al. *Description of the NCAR Community Atmosphere Model (CAM 5.0).* NCAR Technical Note NCAR/TN-486+STR (National Center for Atmospheric Research, 2012).

59. Smith, R. et al. *The Parallel Ocean Program (POP) reference manual: Ocean component of the Community Climate System Model (CCSM) and Community Earth System Model (CESM).* LAUR-10-01853 (Los Alamos National Laboratory, 2010).

60. Oleson, K. W. et al. *Technical Description of version 4.0 of the Community Land Model (CLM).* NCAR Technical Note NCAR/TN-478+STR (National Center for Atmospheric Research, 2010).

61. Lawrence, D. M. et al. Parameterization improvements and functional and structural advances in Version 4 of the Community Land Model. *J. Adv. Model. Earth Syst.* **3**, M03001 (2011).

62. Hunke, E. C. & Lipscomb, W. H. *CICE: the Los Alamos Sea Ice Model Documentation and Software User's Manual Version 4.1.* LA-CC-06-012 (Los Alamos National Laboratory, 2010).

63. Ullrich, P. A. & Zarzycki, C. M. TempestExtremes: a framework for scale-insensitive pointwise feature tracking on unstructured grids. *Geosci. Model Dev.* **10**, 1069–1090 (2017).

64. Ullrich, P. A. et al. TempestExtremes v2.1: a community framework for feature detection, tracking, and analysis in large datasets. *Geosci. Model Dev.* **14**, 5023–5048 (2021).

Author contributions
D.K. and S.-I.A. conceived the idea, guided and supervised the research. S.P. and D.K. designed the study and wrote the first draft of the manuscript. S.P., D.K., H.O., J.S. and B.B.G. performed the analysis. All authors contributed to the interpretation of the results and revision of the manuscript.

Competing interests
The authors declare no competing interests.

Additional information
Supplementary information The online version contains supplementary material available at https://doi.org/10.1038/s41612-024-00858-0.

Correspondence and requests for materials should be addressed to Daehyun Kim or Soon-Il An.

Reprints and permissions information is available at http://www.nature.com/reprints

Publisher's note Springer Nature remains neutral with regard to jurisdictional claims in published maps and institutional affiliations.